

Numerical investigation of lens based setup for depth sensitive diffuse reflectance measurements in an epithelial cancer model

Caigang Zhu and Quan Liu*

Division of Bioengineering, School of Chemical and Biomedical Engineering, Nanyang Technological University,
637457 Singapore
*quanliu@ntu.edu.sg

Abstract: Lens based setups have been explored for non-contact diffuse reflectance measurements to reduce the uncertainty due to inconsistent probe-sample pressure in the past years. However, there have been no reports describing the details of Monte Carlo modeling of lens based non-contact setup for depth sensitive diffuse reflectance measurements to the best of our knowledge. In this study, we first presented a flexible Monte Carlo method to model non-contact diffuse reflectance measurements in a lens based setup. Then this method was used to simulate diffuse reflectance measurements from a squamous cell carcinoma (SCC) tissue model in the cone shell, cone and hybrid configurations, in which the cone shell configuration has not been previously proposed in optical spectroscopy. Depth sensitive measurements were achieved by adjusting the following two parameters: (1) the depth of focal point of the imaging lens in the SCC model; and (2) the cone radius in the cone configuration or the ring radius in the cone shell configuration. It was demonstrated that the cone shell and the hybrid configurations in general have better depth sensitivity to the tumor and the stroma than the more commonly used cone configuration for diffuse reflectance measurements in the SCC model.

©2012 Optical Society of America

OCIS codes: (170.3660) Light propagation in tissues; (170.6510) Spectroscopy, tissue diagnostics; (170.4580) Optical diagnostics for medicine.

References

1. G. Zonios, L. T. Perelman, V. M. Backman, R. Manoharan, M. Fitzmaurice, J. Van Dam, and M. S. Feld, "Diffuse reflectance spectroscopy of human adenomatous colon polyps in vivo," *Appl. Opt.* **38**(31), 6628–6637 (1999).
2. D. Arifler, R. A. Schwarz, S. K. Chang, and R. Richards-Kortum, "Reflectance spectroscopy for diagnosis of epithelial precancer: model-based analysis of fiber-optic probe designs to resolve spectral information from epithelium and stroma," *Appl. Opt.* **44**(20), 4291–4305 (2005).
3. H. W. Wang, J. K. Jiang, C. H. Lin, J. K. Lin, G. J. Huang, and J. S. Yu, "Diffuse reflectance spectroscopy detects increased hemoglobin concentration and decreased oxygenation during colon carcinogenesis from normal to malignant tumors," *Opt. Express* **17**(4), 2805–2817 (2009).
4. U. Utzinger and R. R. Richards-Kortum, "Fiber optic probes for biomedical optical spectroscopy," *J. Biomed. Opt.* **8**(1), 121–147 (2003).
5. Q. Liu, "Role of optical spectroscopy using endogenous contrasts in clinical cancer diagnosis," *World J Clin Oncol* **2**(1), 50–63 (2011).
6. Y. L. Ti and W. C. Lin, "Effects of probe contact pressure on in vivo optical spectroscopy," *Opt. Express* **16**(6), 4250–4262 (2008).
7. R. Reif, M. S. Amoroso, K. W. Calabro, O. A' Amar, S. K. Singh, and I. J. Bigio, "Analysis of changes in reflectance measurements on biological tissues subjected to different probe pressures," *J. Biomed. Opt.* **13**(1), 010502 (2008).
8. J. Delgado Atencio, E. Orozco Guillén, S. Vázquez y Montiel, M. Cunill Rodríguez, J. Castro Ramos, J. Gutiérrez, and F. Martínez, "Influence of probe pressure on human skin diffuse reflectance spectroscopy measurements," *Opt. Mem. Neural. Networks* **18**(1), 6–14 (2009).
9. L. A. Lim, B. Nichols, N. Rajaram, and J. W. Tunnell, "Probe pressure effects on human skin diffuse reflectance and fluorescence spectroscopy measurements," *J. Biomed. Opt.* **16**(1), 011012 (2011).

10. S. Andree, C. Reble, J. Helfmann, I. Gersonde, and G. Illing, "Evaluation of a novel noncontact spectrally and spatially resolved reflectance setup with continuously variable source-detector separation using silicone phantoms," *J. Biomed. Opt.* **15**(6), 067009 (2010).
11. S. F. Bish, N. Rajaram, B. Nichols, and J. W. Tunnell, "Development of a noncontact diffuse optical spectroscopy probe for measuring tissue optical properties," *J. Biomed. Opt.* **16**(12), 120505 (2011).
12. M. Mazurenka, A. Jelzow, H. Wabnitz, D. Contini, L. Spinelli, A. Pifferi, R. Cubeddu, A. D. Mora, A. Tosi, F. Zappa, and R. Macdonald, "Non-contact time-resolved diffuse reflectance imaging at null source-detector separation," *Opt. Express* **20**(1), 283–290 (2012).
13. A. J. Radosevich, N. N. Mutyal, V. Turzhitsky, J. D. Rogers, J. Yi, A. Taflove, and V. Backman, "Measurement of the spatial backscattering impulse-response at short length scales with polarized enhanced backscattering," *Opt. Lett.* **36**(24), 4737–4739 (2011).
14. A. Hielscher, A. Eick, J. Mourant, D. Shen, J. Freyer, and I. Bigio, "Diffuse backscattering Mueller matrices of highly scattering media," *Opt. Express* **1**(13), 441–453 (1997).
15. E. Vitkin, V. Turzhitsky, L. Qiu, L. Guo, I. Itzkan, E. B. Hanlon, and L. T. Perelman, "Photon diffusion near the point-of-entry in anisotropically scattering turbid media," *Nat Commun* **2**, 587 (2011).
16. V. Turzhitsky, N. N. Mutyal, A. J. Radosevich, and V. Backman, "Multiple scattering model for the penetration depth of low-coherence enhanced backscattering," *J. Biomed. Opt.* **16**(9), 097006 (2011).
17. L. V. Wang and G. Liang, "Absorption distribution of an optical beam focused into a turbid medium," *Appl. Opt.* **38**(22), 4951–4958 (1999).
18. L. H. Wang, S. L. Jacques, and L. Q. Zheng, "Mcm - Monte-Carlo Modeling of Light Transport in Multilayered Tissues," *Comput Meth Prog Bio* **47**(2), 131–146 (1995).
19. B. L. Allen-Hoffmann, S. J. Schlosser, C. A. R. Ivarie, C. A. Sattler, L. F. Meisner, and S. L. O'Connor, "Normal growth and differentiation in a spontaneously immortalized near-diploid human keratinocyte cell line, NIKS," *J. Invest. Dermatol.* **114**(3), 444–455 (2000).
20. C. G. Zhu and Q. Liu, "Validity of the semi-infinite tumor model in diffuse reflectance spectroscopy for epithelial cancer diagnosis: a Monte Carlo study," *Opt. Express* **19**(18), 17799–17812 (2011).
21. D. C. Walker, B. H. Brown, A. D. Blackett, J. Tidy, and R. H. Smallwood, "A study of the morphological parameters of cervical squamous epithelium," *Physiol. Meas.* **24**(1), 121–135 (2003).
22. C. Kortun, Y. R. Hijazi, and D. Arifler, "Combined Monte Carlo and finite-difference time-domain modeling for biophotonic analysis: implications on reflectance-based diagnosis of epithelial precancer," *J. Biomed. Opt.* **13**(3), 034014 (2008).
23. S. K. Chang, D. Arifler, R. Drezek, M. Follen, and R. Richards-Kortum, "Analytical model to describe fluorescence spectra of normal and preneoplastic epithelial tissue: comparison with Monte Carlo simulations and clinical measurements," *J. Biomed. Opt.* **9**(3), 511–522 (2004).
24. K. B. Sung and H. H. Chen, "Enhancing the sensitivity to scattering coefficient of the epithelium in a two-layered tissue model by oblique optical fibers: Monte Carlo study," *J. Biomed. Opt.* **17**(10), 107003 (2012).
25. Q. Liu and N. Ramanujam, "Experimental proof of the feasibility of using an angled fiber-optic probe for depth-sensitive fluorescence spectroscopy of turbid media," *Opt. Lett.* **29**(17), 2034–2036 (2004).
26. T. J. Pfefer, A. Agrawal, and R. A. Drezek, "Oblique-incidence illumination and collection for depth-selective fluorescence spectroscopy," *J. Biomed. Opt.* **10**(4), 044016 (2005).
27. Q. Liu and N. Ramanujam, "Sequential estimation of optical properties of a two-layered epithelial tissue model from depth-resolved ultraviolet-visible diffuse reflectance spectra," *Appl. Opt.* **45**(19), 4776–4790 (2006).
28. R. Drezek, K. Sokolov, U. Utzinger, I. Boiko, A. Malpica, M. Follen, and R. Richards-Kortum, "Understanding the contributions of NADH and collagen to cervical tissue fluorescence spectra: modeling, measurements, and implications," *J. Biomed. Opt.* **6**(4), 385–396 (2001).
29. J. Qu, C. Macaulay, S. Lam, and B. Palcic, "Optical properties of normal and carcinomatous bronchial tissue," *Appl. Opt.* **33**(31), 7397–7405 (1994).
30. A. M. J. Wang, J. E. Bender, J. Pfefer, U. Utzinger, and R. A. Drezek, "Depth-sensitive reflectance measurements using obliquely oriented fiber probes," *J. Biomed. Opt.* **10**(4), 044017 (2005).
31. R. A. Schwarz, W. Gao, D. Daye, M. D. Williams, R. Richards-Kortum, and A. M. Gillenwater, "Autofluorescence and diffuse reflectance spectroscopy of oral epithelial tissue using a depth-sensitive fiber-optic probe," *Appl. Opt.* **47**(6), 825–834 (2008).

1. Introduction

Diffuse reflectance spectroscopy has been investigated for the early diagnosis of epithelial cancer in the past two decades [1–3]. Due to its non-invasiveness and capability to provide quantitative information about the physiological and pathological status of tissues in real time, this technique has great potential to be widely used in clinical settings. In a typical diffuse reflectance setup, a fiber-optic probe serves as the conduit for the delivery of illuminating light and collection of emitted light [4]. The fiber-optic probe is a metal cylindrical tube enclosing one or multiple optical fibers [5], in which some fibers are used for delivering light onto a tissue surface and the same fibers or other fibers depending on the probe design are used for collecting light emanating from the tissue surface.

Although fiber-optic probes are widely used in optical spectroscopy due to their flexibility and high efficiency [4], the uncertainty in measurements due to inconsistent probe-sample pressure is difficult to remove. It has been reported that the inconsistent pressure could induce significant distortions in measured spectra, which consequently would cause large errors in diagnosis [6–9]. To reduce such an artifact, several groups have developed lens based setups for non-contact diffuse reflectance measurements. Andree et al [10] reported a lens based setup involving a spherical and a flat folding mirror for illumination while two achromatic lenses for detection. An illumination fiber was placed at the focal point of the spherical mirror to deliver the white light to tissue surface. A detection fiber was placed at the focal point of the top achromatic lens to transmit diffusely scattered light to a spectrometer. The distance between the illumination and the detection area can be varied continuously; moreover, both source and detection fibers with different diameters can be used. Therefore this non-contact lens based setup is able to perform spatially resolved diffuse reflectance measurements without physically contacting a tissue sample. Bish et al [11] recently proposed a different setup for non-contact diffuse reflectance measurements. Two collimating lenses were used to image the illumination and collection fibers onto the tissue surface and serve as a non-contact probe to eliminate the influence of inconsistent probe-tissue pressure that would be present in a contact probe. To overcome the limit of the lens in focal depth, a customized autofocus mechanism was incorporated in the setup. Mazurenka et al [12] introduced a non-contact lens based setup for time-resolved diffuse reflectance measurements, in which laser scanning was used to achieve imaging. Besides the reports reviewed above, some other proposed techniques such as low coherence enhanced backscattering [13], diffuse backscattering [14], and confocal technique [15] have also been explored for non-contact diffuse reflectance measurements. Turzhitsky et al [16] examined the dependence of the penetration depth of low coherence enhanced backscattering signals on optical properties using Monte Carlo modeling, but they did not look into the details on the simulation of lens based illumination and detection.

The literature review above demonstrates that the lens based setup is a promising tool for non-contact diffuse reflectance measurements without distortion due to inconsistent probe-sample contact. However, there have been no reports describing the details of Monte Carlo modeling of lens based non-contact setup for depth sensitive diffuse reflectance measurements to the best of our knowledge. In this study, we first presented a Monte Carlo method to model non-contact diffuse reflectance measurements in a lens based setup with a cone or cone shell configuration. Then this method was used to simulate diffuse reflectance measurements from a squamous cell carcinoma (SCC) tissue model in the cone shell, cone and hybrid configurations, in which the cone shell configuration has not been previously proposed in optical spectroscopy. The performance of three configurations in terms of the sensitivity to the tumor and the stroma was compared to each other.

2. Monte Carlo method for non-contact lens based setup

2.1 Lens based non-contact diffuse reflectance measurement setup

The schematic of the proposed lens based set up is shown in Fig. 1(a). White light from a point source, i.e. S, was first collimated by Lens 1 into a polarizing cube beam splitter, and then focused into a tissue sample via Lens 2. Note that Lens 2 is also called the imaging lens in this paper according to its role in measurements. Diffusely reflected light from the tissue sample was collected by Lens 2 and collimated into the polarizing cube beam splitter, which was then focused into a detection fiber by Lens 3. The detection fiber would deliver the light into a spectrometer. The polarizing cube beam splitter reflected one component of light with a particular polarization, for example the S component, while allowing the other component of light, for example the P component, to transmit through. The role of the beam splitter in this setup was to minimize the contribution of specular reflectance. Lenses 2 and 3 were assumed to possess equal focal distances. The shape of the intersection between light and the sample volume in an optically transparent sample is typically a cone, in which case light intersecting

with the plane of Lens 2 forms a circle as shown in the top graph of Fig. 1(b). In this study, we would like to propose a configuration, in which the shape of intersection between light and sample volume is a cone shell and consequently light intersecting with the plane of Lens 2 forms a ring as shown in the bottom graph of Fig. 1(b).

In practice, a mask can be placed between the beam splitter and Lens 2 to change the dimensions of the cone or cone shell configuration. For example, a diaphragm serving as the mask can be used to control the radius of the circle in the cone configuration, i.e. r in Fig. 1(b); while a ring slider with multiple rings each having different dimensions as the mask can be used to control the ring dimensions including the ring radius R and the thickness t in the cone shell configuration. Note that both illumination and detection are affected by the mask in Fig. 1(a) because it is located right next to the imaging lens, i.e. Lens 2. If a ring slider is placed between Lens 1 and the beam splitter and a diaphragm is placed between Lens 3 and the beam splitter at the same time, this will create a hybrid configuration with the cone shell configuration for illumination and the cone configuration for detection.

The sample stage can be moved up and down to vary the imaging depth. Alternatively, Lens 2 can be adjusted to change the depth of focal point in the tissue sample and achieve the same purpose. In principle, most non-contact setups for diffuse reflectance spectroscopy mentioned earlier are similar to this setup in terms of the illumination and detection configuration. In this sense, the methodology and most results in this study are generally applicable to many other non-contact lens based systems for diffuse reflectance measurements.

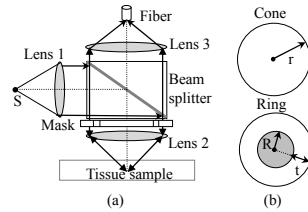


Fig. 1. (a) Schematic of the lens based set up for non-contact diffuse reflectance measurements; (b) The circular (top) and ring (bottom) shapes of the mask between Lens 2 and the beam splitter in the cone and cone shell configurations. In (b), light can pass through the white area but is blocked in the gray area. The symbols, “ r ”, “ R ” and “ t ” represent the radius of the circle in the cone configuration, and the ring radius and the ring thickness in the cone shell configuration. The cone configuration can be seen as a special case of cone shell configuration in which the ring radius is zero.

2.2 Cone shell illumination in Monte Carlo simulation

Monte Carlo method for simulating focused light beam, i.e. the cone configuration for illumination, has been described by Wang et al [17], in which the detection configuration was not considered. In this study, Wang’s method is extended from the cone illumination to the cone shell illumination; then a numerical method is developed to simulate the cone shell detection.

Only the cone shell configuration is described here because the cone configuration can be treated as a special case of the cone shell configuration in which the ring radius is zero. The ring radius, ring thickness, the imaging lens’s focal length and the depth of focal point in the tissue can uniquely define a cone shell configuration. The four parameters were denoted by R , t , f and Z_f respectively. It should be noted that the maximum value of R cannot be larger than the radius of lens. The lens used here was treated ideal thus the lens thickness was not taken into account. A Cartesian coordinate system was set up in the simulation to facilitate tracking the positions of photons. The origin was the center of the incident light beam on the surface of the tissue model. The Z axis was the normal of the surface pointing toward the inside of the turbid. The x - y plane was located on the surface of the tissue model. The focused light beam formed a ring with a radius of ρ_{ring} and a thickness of t_{new} on the tissue surface as shown in

Fig. 2. The radius and thickness of the illumination ring on the tissue surface can be calculated from R and t as follows.

$$\frac{\rho_{ring}}{R} = \frac{Z_f}{f} \quad (1)$$

$$\frac{t_{new}}{t} = \frac{Z_f}{f} \quad (2)$$

The irradiance was assumed to be uniform on the surface of the turbid medium and the radial position of a photon packet was sampled by

$$\rho = \sqrt{[(\rho_{ring} + t_{new})^2 - \rho_{ring}^2] \mathcal{E}_\rho + \rho_{ring}^2} \quad (3)$$

where \mathcal{E}_ρ was a random number uniformly distributed between 0 and 1. The azimuthal angle of the photon packet was sampled by

$$\theta = 2\pi\mathcal{E}_\theta \quad (4)$$

where \mathcal{E}_θ was a random number uniformly distributed between 0 and 1. The Cartesian coordinates of the incident point were then

$$x = \rho \cos(\theta) \quad (5)$$

$$y = \rho \sin(\theta) \quad (6)$$

The directional cosines were set to

$$u_x = -x / \sqrt{\rho^2 + Z_f^2} \quad (7)$$

$$u_y = -y / \sqrt{\rho^2 + Z_f^2} \quad (8)$$

$$u_z = Z_f / \sqrt{\rho^2 + Z_f^2} \quad (9)$$

If the ambient medium and the tissue had the same refractive index, the directional cosines did not need to change when the photon entered the tissue. Otherwise, the directional cosines were changed based on the Snell's law and the specular reflection was taken into account based on the Fresnel law. Once the photon was launched into the tissue model, the treatment of photon tracing was exactly same as that done by Wang et al [18] thus was not repeated here.

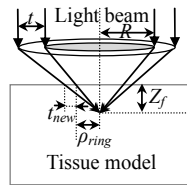


Fig. 2. Cone shell illumination schematic.

2.3 Cone shell detection in Monte Carlo simulation

Besides the parameters associated with the lens mentioned above, i.e. R , t , f and Z_f (Fig. 2), two additional parameters associated with the detection fiber (Fig. 1), including the fiber diameter and the numerical aperture (NA), were also used to define the cone shell detection. The detection part of the setup can be simplified as shown in Fig. 3(a).

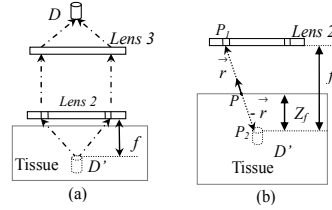


Fig. 3. (a) Schematic of the cone shell detection; (b) Detailed view of the cone shell detection at the interface of Lens 2 and the tissue model.

To simplify the problem, the thickness of the mask was assumed to be zero. Since both the imaging lens and the mask were treated as infinitely thin, the two components can be merged into Lens 2 as shown in Fig. 3(a). The detection fiber D is placed at the focal plane of Lens 3. An image of the fiber D can be formed in the tissue model on the focal plane of Lens 2, which is denoted as D' in Fig. 3(a). Because Lenses 2 and 3 possess equal focal distances, D and D' have equal size. Due to the reciprocity of ray tracing, finding whether a photon is detected by fiber D is equivalent to identifying whether the photon can be traced back to its image D' and the latter problem is easier to solve. Figure 3(b) illustrates the detail about how an exiting photon can be traced back to D'. Once a photon exits the tissue surface in a direction of \vec{r} from position P, two steps will be performed to determine whether this photon could be detected by the detector. The first step is to determine whether this photon can pass through the ring. This can be done by moving the photon from P to the plane of Lens 2 along \vec{r} and find the intersection with the plane of Lens 2, which is denoted by P₁. If P₁ is located within the ring, it suggests that the photon can pass through the ring then the photon will continue to go through the second step, otherwise the detection procedure for this photon will be terminated. The second step is to perform ray retracing to determine whether this photon could be detected by the detection fiber. This can be done by moving the photon from P along vector $-\vec{r}$ towards the plane of $Z = Z_f$ and checking whether the intersection with the plane, which is denoted by P₂, is located within the fiber tip area. If it is, the exiting angle of this photon will be compared to the acceptance angle of the fiber, which is calculated from the NA value. If the exiting angle is also smaller than the fiber acceptance angle, the photon will be counted as being detected by the fiber; otherwise the photon will be rejected. If a photon is detected by the fiber, all related trajectory information will be recorded. It should be noted that the mismatch of refractive indices of the tissue model and the ambient medium above the tissue does not affect the ray retracing step proposed above. This is due to the fact that D' was an image of D. In the retracing procedure, the virtual medium around D', which is the "image" of the medium around D, should have the same refractive index as that of the medium around D, which happens to be equal to the refractive index of the ambient medium above the tissue.

2.4 Validation of the Monte Carlo method

To validate the Monte Carlo method introduced above, several simulations were performed. The illumination scheme described above was validated against results published by Wang et al [17], in which the agreement between our results and published ones was excellent (results not shown to save space).

To validate the detection scheme, we performed another set of simulations in a semi-infinite homogeneous tissue model. The optical properties of the tissue model were $n_t = 1.4$, $\mu_a = 1.0 \text{ cm}^{-1}$, $\mu_s = 100 \text{ cm}^{-1}$, and $g = 0.9$. The refractive index of the ambient medium was also set to 1.4 such that there was no refractive index mismatch on the top surface of the tissue model. The diameter of the detection fiber was 2 mm and the NA was set to 0.6. The radii of lenses 2 and 3 were 10 mm while the focal lengths were set to 20 mm. Both the ring radius and the ring thickness were set to 5 mm. The depth of focal point of the imaging lens, i.e. Lens 2, in the tissue model was varied from 0.5 mm to 1.0 mm at an increment of 0.5 mm. In each simulation, 200 million photons were launched and the grid sizes were 0.04 mm in x,

y, and z dimensions. The absorption distribution contributed only by detected photons was shown in Fig. 4. Figure 4(a) shows the result for the first simulation in which the depth of focal point in tissue was 0.5 mm. Based on the setting described above, the light beam focused onto the turbid medium surface should form a ring with a radius of 0.125 mm and a ring thickness of 0.125 mm. Figure 4(a) shows that, the shape and size of light beam focused onto the medium surface approximately agree with our predictions, in which the blurred boundary of the cone shell was due to the turbidity of the tissue model. It is also clear that the brightest spot in the tissue model is located at a depth of around 0.5 mm, which agrees with the depth of the focal point in the tissue model set in the simulation parameters. The result for the other situation, i.e. when the depth of the focal point in the tissue model was 1.0 mm, was shown in Fig. 4(b). Based on the setting for this situation, the light beam focused onto the turbid medium surface should form a ring with a radius of 0.25 mm and a ring thickness of 0.25 mm. Figure 4(b) shows that, the shape and size of light beam focused onto the medium surface approximately agree with our predictions. It can be observed that there was no single obvious focus in the absorption distribution and the distribution shifted towards the superficial area. Moreover the bottom edge of the absorption distribution was located around 0.8 mm, which was likely due to the joint effects of tissue turbidity and the cone shell detection scheme. Based on the results shown in Fig. 4, it can be seen that the Monte Carlo method for the cone shell configuration of illumination and detection has been validated.

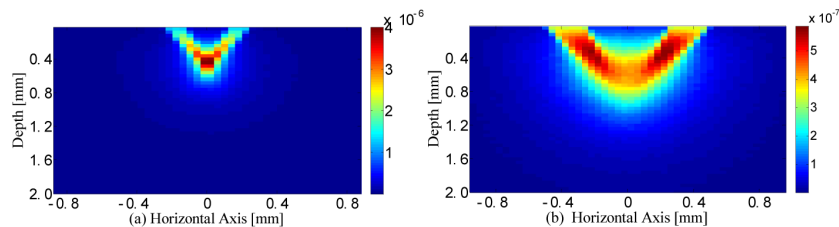


Fig. 4. Absorption distribution of detected photons for (a) the depth of focal point in the tissue model was 0.5 mm; and (b) the depth of focal point in the tissue model was 1.0 mm.

3. Depth sensitive diffuse reflectance measurements in epithelial cancer model

3.1 Early Squamous Cell Carcinoma model

An epithelial tissue typically consists of two layers, the top epithelium and the bottom stroma. The basement membrane separates the two layers. The squamous cell carcinoma (SCC) usually originates from the basement membrane of the epithelium [19]. Previously our group has utilized a simplified early squamous cell carcinoma model in which the SCC tumor is assumed to be a cuboid target whose dimensions and position can be specified [20]. The actual dimensions and position of an SCC tumor in an epithelial tissue varied considerably among stages during tumor development. The SCC model used in this study is shown in Fig. 5. The epithelial thickness was set to 0.5 mm [21]. The stromal thickness was set to 2.5 mm to represent a semi-infinite layer. The tumor width and length were both set to 0.5 mm and the tumor thickness was set to 0.3 mm. This SCC model represents a tumor model in an early stage. The optical properties of each region as listed in Table 1 were obtained from the literature [22] at a wavelength of 420 nm. This wavelength was chosen because it is close to the absorption peak of hemoglobin, which is the major absorber in human tissues. A refractive index of 1.4 was used in all tissue regions [23]. The anisotropy factors of the epithelium and the tumor were set to 0.97 and an anisotropy factor of 0.8 was used for the stroma [23].

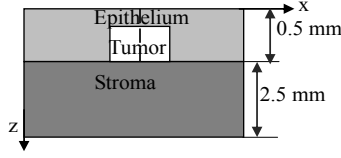


Fig. 5. Cross section view of the squamous cell carcinoma (SCC) tissue model. The tumor width and length were set to 0.5 mm while the tumor thickness was set to 0.3 mm. This model represents a tumor in an early stage.

Table 1. Optical properties of the SCC tissue model at 420nm ^[22]

Tissue	Optical properties		
	$\mu_a(cm^{-1})$	$\mu_s(cm^{-1})$	g
Epithelium	3.0	42.4	0.97
Tumor	3.0	127.2	0.97
Stroma	9.09	266.3	0.8

Note: μ_a : absorption coefficient; μ_s : scattering coefficient; g : anisotropy

3.2 Criteria for the evaluation of depth sensitivity in a non-contact setup

To characterize the depth sensitivity of the non-contact set up, two criteria that have been reported previously [24] were used. The first criterion was the weighted fraction of photon-scatterer collisions for detected photons, which is mainly determined by the scattering properties of the tissue model, spent in each region. The numbers of photon-scatterer collisions in the epithelium, the SCC and the stroma were recorded separately for each detected photon, and then the weighted average number of collisions in the each region can be calculated as follows:

$$\overline{NC} = \frac{\sum_{i=1}^N W_i * NC_i}{\sum_{i=1}^N W_i} \quad (10)$$

where W_i is the exit weight of each detected photon, NC_i is the number of collision spent in the region and N is the total number of detected photons. The fraction of collisions spent in the tumor (FCT) was obtained according to the following equation:

$$FCT = \frac{\overline{NC}_{tumor}}{\overline{NC}_{epithelium} + \overline{NC}_{tumor} + \overline{NC}_{stroma}} \quad (11)$$

The fraction of collisions spent in the epithelium (FCE) and the stroma (FCS) can be obtained similarly. The second criterion was the weighted fraction of path length spent in each region for detected photons. The path length of each detected photon spent in the epithelium, the SCC and the stroma were recorded, and then the weighted average photon path length in each region for all detected photons can be calculated as follows:

$$\overline{PL} = \frac{\sum_{i=1}^N W_i * PL_i}{\sum_{i=1}^N W_i} \quad (12)$$

where W_i is the exit weight of each detected photon, PL_i is the path length spent in the region and N is the total number of detected photons. The fraction of path length spent in the tumor (FPLT) was obtained by:

$$FPLT = \frac{\overline{PL_{tumor}}}{\overline{PL_{epithelium}} + \overline{PL_{tumor}} + \overline{PL_{stroma}}} \quad (13)$$

The fraction of path length spent in epithelial (FPLE) and in the stroma (FPLS) can be obtained similarly.

3.3 Simulation parameters for the cone shell, the cone, and the hybrid configurations

To investigate the depth sensitivity of each configuration in diffuse reflectance measurements, a series of simulations were performed on the SCC model. In all simulations, the refractive index of the ambient medium was set to 1.0 that represented the refractive index of air, both the radius and the focal length of the imaging lens were set to 10 mm thus the half angle of light cone formed by the lens was 45 degrees for incident light, the NA value of the detection fiber was set to 1.0 to increase the efficiency of photon detection without losing generality. The central line of the Lens 2 and Lens 3 (Fig. 1) always overlap with the middle line of the tumor (dashed line shown in Fig. 5). The parameters investigated in the simulations for the cone shell configuration, the cone configuration and the hybrid configuration involving the cone shell illumination and cone detection, were listed in Tables 2, 3 and 4 respectively. It should be noted that the cone radius for detection in the hybrid configuration was always equal to the radius of the lens, i.e. 10 mm. In each independent simulation, 10 million photons were used, which was repeated five times to estimate the means and standard deviations for the construction of error bars shown in the results section.

Table 2. Simulations for the cone shell configuration

Parameters	Values under investigation
Ring radius (mm)	0, 2, 4, 6
Ring thickness (mm)	1, 2, 3
Depth of focal point in tissue (mm)	0.1, 0.3, 0.5, 1.0
Detection fiber diameter (mm)	0.1, 0.2, 0.4

Table 3. Simulations for the cone configuration

Parameters	Values under investigation
Cone radius (mm)	2, 4, 6, 8
Depth of focal point in tissue (mm)	0.1, 0.3, 0.5, 1.0
Detection fiber diameter (mm)	0.1, 0.2, 0.4

Table 4. Simulations for the hybrid configuration*

Parameters	Values under investigation
Ring radius (mm)	0, 2, 4, 6
Ring thickness (mm)	1, 2, 3
Depth of focal point in tissue (mm)	0.1, 0.3, 0.5, 1.0
Detection fiber diameter (mm)	0.1, 0.2, 0.4

*Note: The cone radius for detection in the hybrid configuration was always equal to the radius of the lens, i.e. 10 mm

4. Results

4.1 Diffuse reflectance intensity and depth sensitivity in the cone shell configuration

Simulated diffuse reflectance intensity from the SCC tissue model as a function of the ring radius for the cone shell configuration is shown in Fig. 6. The error bars associated with most data points in Fig. 6 are too small to see. An overall decreasing trend in diffuse reflectance with increasing ring radii can be observed. This is expected because an increasing ring radius would result in a longer photon path thus detected photons would experience larger

attenuation. A depth of 0.3 mm for the focal point in the tissue model produces the highest diffuse reflectance intensity in all cases. In contrast, a depth of 1 mm produces the lowest diffuse reflectance intensity.

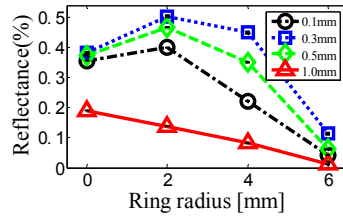


Fig. 6. Diffuse reflectance as a function of the ring radius for a range of depths of the focal point in the tissue model in a cone shell configuration. Each line represents the results for a different depth value as indicated in the legends. The ring thickness and the diameter of detection fiber were fixed at 2 mm and 0.2 mm, respectively.

Figure 7 shows the fraction of collisions spent in the tumor, the epithelium and the stroma for the cone shell configuration. Figure 7(a) suggests that the fraction of collisions in the tumor does not change considerably when the depth of focal point in the tissue model is varied from 0.1 mm to 0.5 mm; however it drops significantly when the depth value is increased to 1.0 mm. A depth value of 0.3 mm with a large ring radius, i.e. 6 mm in Fig. 7(a), yields the most significant contribution from the tumor. Figure 7(c) shows that the fraction of collisions in the stroma increases significantly when the ring radius is increased for the depth of 1.0 mm. The largest ring radius at 6 mm produces the highest collision fraction, i.e. around 73%, from the stroma. The fraction of collisions in the epithelium is significantly affected by the finite width of the tumor. When a small ring radius close to zero is used, the SCC model can be treated as three layers including the thin epithelium, for which a smaller focus depth produce higher collision fraction in the epithelium. When a larger ring radius is used, the trajectory of most detected photons may get around the tumor. In this case, the SCC model could be treated as two layers including the thick epithelium and the stroma only thus the trend becomes quite different.

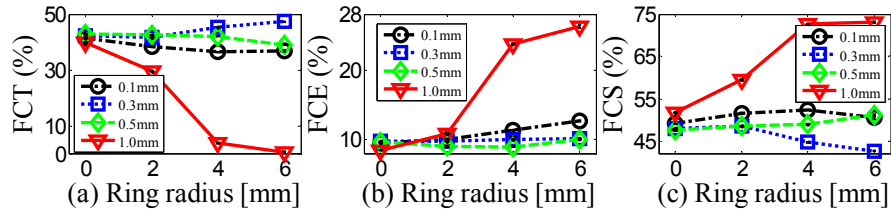


Fig. 7. Fraction of collisions in (a) the tumor, (b) the epithelium and (c) the stroma layer in the cone shell configuration. Each line represents the results for a different depth value as indicated in the legends. The ring thickness and the diameter of detection fiber were fixed at 2 mm and 0.2 mm, respectively.

Figure 8 shows the fractions of path length spent in the tumor, epithelium and stroma in the cone shell configuration. It is easy to see that the trends in Fig. 8 agree with those shown in Fig. 7. Therefore only the fraction of collisions spent in each region will be shown in the subsequent sections to represent the depth sensitivity of the non-contact setup.

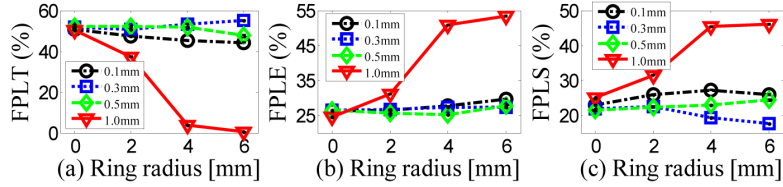


Fig. 8. Fraction of path length in (a) the tumor, (b) the epithelium and (c) the stroma layer in the cone shell configuration. Each line represents the results for a different depth value as indicated in the legends. The ring thickness and the diameter of detection fiber were fixed at 2 mm, and 0.2 mm respectively.

4.1.1 Effect of the ring thickness on the depth sensitivity of the cone shell configuration

Because it has been found that the depths of focal point of 0.3 mm and 1.0 mm yield the best sensitivity for the tumor and stroma respectively, only the FCT for a depth of 0.3 mm and the FCS for a depth of 1.0 mm are shown below. The effects of ring thickness on the depth sensitivity for cone shell configuration were shown in Fig. 9. It can be found that the FCT and FCS did not change too much when the ring thickness varied.

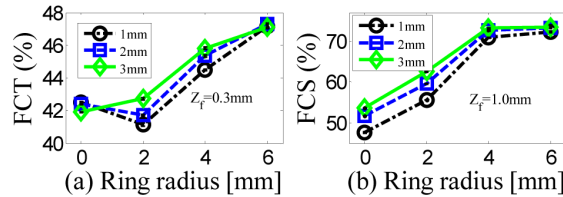


Fig. 9. Effect of the ring thickness on the fraction of collisions in (a) the tumor and (b) the Stroma for the cone shell configurations. In (a), the depth of focal point in the tissue model, i.e. Z_f , is 0.3 mm; while in (b), the depth of focal point in the tissue model, i.e. Z_f , is 1.0 mm. Each line represents the results for a different ring thickness as indicated in the legends. The diameter of detection fiber was fixed at 0.2 mm.

4.1.2 Effect of the detection fiber size on the depth sensitivity of the cone shell configuration

The effect of the detection fiber size on the depth sensitivity of the cone shell configuration was shown in Fig. 10. It can be seen from Fig. 10(a) that, a smaller detection fiber size always provides a higher fraction of collision in the tumor. In Fig. 10(b), an opposite trend is observed but the changes in the fractions in the stroma are insignificant.

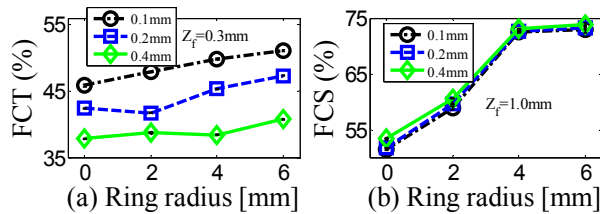


Fig. 10. Effect of the detection fiber size on the fraction of collisions in (a) the tumor and (b) the Stroma for the cone shell configurations. In (a), the depth of focal point in the tissue model, i.e. Z_f , is 0.3 mm; while in (b), the depth of focal point in the tissue model, i.e. Z_f , is 1.0 mm. Each line represents the results for a different detection fiber size as indicated in the legends. The ring thickness was fixed at 2 mm.

4.2 Depth sensitivity in the cone configuration

The depth sensitivity for the cone configuration in both illumination and detection is shown in Fig. 11. Figure 11(a) shows that a smaller detection fiber size always provides a higher

fraction of collisions in the tumor region. Figure 11(b) shows that the changes in the fraction of collisions in the stroma are insignificant.

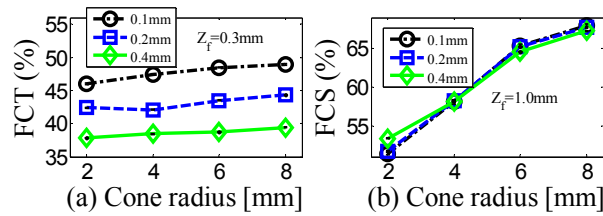


Fig. 11. Effect of the detection fiber size on the fraction of collisions in (a) the tumor and (b) the Stroma for the cone configurations. In (a), the depth of focal point in the tissue model, i.e. Z_f , is 0.3 mm; while in (b), the depth of focal point in the tissue model, i.e. Z_f , is 1.0 mm. Each line represents the results for a different detection fiber size as indicated in the legends.

4.3 Depth sensitivity in a hybrid configuration with the cone shell illumination and cone detection

Figure 12 shows the effect of the ring thickness on the depth sensitivity of the hybrid configuration. Figure 12 shows that a larger ring thickness provides a slightly higher fraction of collisions in the tumor region and the stroma, but the changes in the fraction of collisions are not significant.

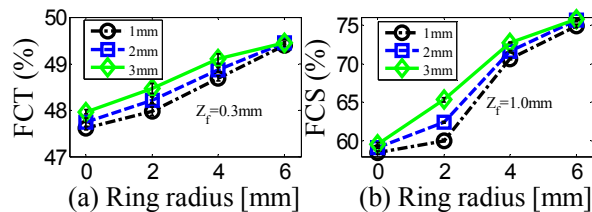


Fig. 12. Effect of the ring thickness on the fraction of collisions in (a) the tumor and (b) the stroma for the hybrid configuration. In (a), the depth of the focal point in the tissue model, i.e. Z_f , is 0.3 mm; while in (b), the depth of the focal point is 1.0 mm. Each line represents the results for a different ring thickness as indicated by the legends. The diameter of the detection fiber was fixed at 0.2 mm. The radius of the cone for detection is equal to the radius of the imaging lens, i.e. 10 mm.

Figure 13 demonstrates the effect of the size of the detection fiber on the depth sensitivity of the hybrid configuration. Figure 13(a) shows that a smaller detection fiber size always provides a higher collision fraction in the tumor region. Figure 13(b) illustrates a similar trend in the fraction of collisions in the stroma but the changes are insignificant.

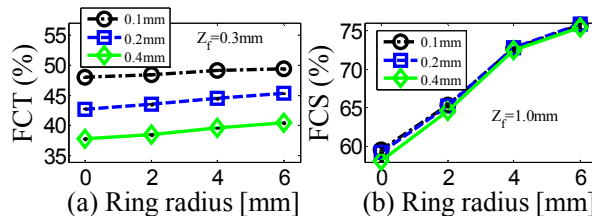


Fig. 13. Effect of the detection fiber size on the fraction of collisions in (a) the tumor and (b) the stroma for the hybrid configuration. In (a), the depth of the focal point in the tissue model, i.e. Z_f , is 0.3 mm; while in (b), the depth of the focal point is 1.0 mm. Each line represents a different size of the detection fiber as indicated by the legends. The ring thickness was fixed at 3 mm. The radius of the cone for detection is equal to the radius of the imaging lens, i.e. 10 mm.

4.4 Comparison of depth sensitivity between the cone shell, cone and hybrid configuration

Tables 5 and 6 show the comparison of the best sensitivity between all above configurations for the tumor and the stroma, respectively. The data in the table are extracted from relevant figures shown earlier. Besides FCT and FCS, a new criterion, i.e. tumor contrast (TC), is included to evaluate the sensitivity to tumor because of the general interest in tumor detection. The tumor contrast (TC) is defined as the percent deviation for diffuse reflectance which was calculated based on Eq. (14),

$$TC = \frac{|R_{tumor} - R_{control}|}{R_{control}} \times 100\% \quad (14)$$

where R_{tumor} is the diffuse reflectance simulated from the tumor model and $R_{control}$ is the diffuse reflectance simulated from the control tissue model. The two models are exactly identical except that there is no tumor buried in the epithelial layer in the control tissue model. Table 5 shows that there was no significant difference between any two of the three configurations in terms of FCT. However, the hybrid configuration and cone shell configuration performed noticeably better than the commonly used cone configuration in terms of TC. Table 6 shows that the hybrid configuration and cone shell configuration yielded similar FCS for the stroma, and they both performed better than the commonly used cone configuration

Table 5. The best FCT between the cone, the hybrid and the cone shell set up for a depth of focus of 0.3 mm

Configuration		Cone	Hybrid	Cone shell
Specifications	Radius	8 mm	6 mm	6 mm
	Detector size	0.1 mm	0.1 mm	0.1 mm
	Ring thickness	NA	3 mm	2 mm
FCT		49% ± 0.1%	49% ± 0.1%	51% ± 0.1%
TC		24.9% ± 0.4%	29.9% ± 0.4%	31.0% ± 0.6%

Note: FCT: The fraction of collisions in the tumor; NA: Not applicable; TC: tumor contrast. The row header "radius" refers to the cone radius in the cone configuration and the ring radius in both the cone shell configuration and hybrid configuration. In the rows of "FCT" and "TC", the first percentage is the mean while the second percentage is the standard deviation of the corresponding quantity.

Table 6. The best FCS between the cone, the hybrid and the cone shell set up for a depth of focus of 1.0 mm

Configuration		Cone	Hybrid	Cone shell
Specifications	Radius	8 mm	6 mm	6 mm
	Detector size	0.1 mm	0.4 mm	0.4 mm
	Ring thickness	NA	3 mm	3 mm
FCS		68% ± 0.2%	76% ± 0.2%	74% ± 0.1%

Note: FCS: The fraction of collisions in the stroma; NA: Not applicable. The row header "radius" refers to the cone radius in the cone configuration and the ring radius in both the cone shell configuration and hybrid configuration. In the rows of "FCS", the first percentage is the mean while the second percentage is the standard deviation of the corresponding quantity.

5. Discussion

The findings shown in the results section can be explained by considering the light transport in the tissue model as follows.

Figure 6 shows simulated diffuse reflectance as a function of the ring radius for a range of depths of focal point in the tissue model for the cone shell configuration. A depth of 0.3 mm produces the highest diffuse reflectance intensity in all cases, while a depth of 1 mm yields the lowest diffuse reflectance due to the larger attenuation associated with the longer photon path length in this case. Because a depth of 1 mm happens to yield a high sensitivity to the

stroma according to Figs. 7 and 8, a tradeoff will have to be made between the diffuse reflectance intensity and the sensitivity to the stroma for the choice of the depth value. A similar tradeoff needs to be made between the diffuse reflectance intensity and the sensitivity to the tumor for the choice of the ring radius in the cone shell configuration. In contrast, no tradeoff needs to be made for the choice of the depth value for the tumor because a depth of 0.3 mm yields both high sensitivity to the tumor and high diffuse reflectance intensity.

Figure 7 shows that depth sensitive diffuse reflectance measurements could be achieved by adjusting: (1) the depth of the focal point in the tissue model; and (2) the cone radius in the cone configuration or ring radius in the cone shell configuration. When the focal point of the imaging lens is located inside the tumor, e.g. $Z_f = 0.3$ mm, most launched photons can reach and travel in the tumor region and the fraction of collisions spent in tumor is large. When the focal point is located in the stroma, e.g. $Z_f = 1.0$ mm, most launched photons travel around the tumor and reach the stroma due to the high anisotropy factor of the tumor and the epithelium, i.e. 0.97. Consequently the fraction of collisions spent in the tumor is very small and the fraction of collisions spent in the stroma is large. It is observed in Fig. 7(a) that a larger ring radius yields a higher tumor collision fraction for a depth of the focal point of 0.3 mm. The opposite trend is observed for a depth of 1.0 mm. This phenomenon can be explained by Fig. 14, in which the intersection between the cone shell region and tumor drawn in black determines the contribution of the tumor to measured diffuse reflectance. As shown in Fig. 14(a), a focal point with a depth of 0.3 mm is located inside the tumor region. When the ring radius is increased, the intersection of the cone shell region and the tumor, i.e. the black area in Fig. 14(a), increases thus the fraction of collisions of detected photons spent in the tumor would increase accordingly. For a focal point with a depth of 1.0 mm, the beam can get around the central portion of the tumor and reach the tumor as shown in Fig. 14(b). The intersection between the cone shell region and the tumor is small thus few detected photons travel through the tumor. That explains the small fraction of collisions in the tumor when the depth of the focal point is 1.0 mm. The results for the fraction of collisions in the stroma as in Fig. 7(c) can be explained in a similar way.

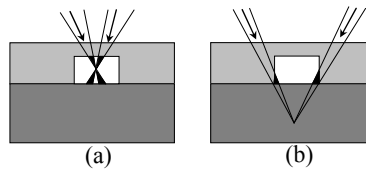


Fig. 14. Intersection of the cone shell region and the tumor when the depth of the focal point in the tumor model is (a) 0.3 mm and (b) 1.0 mm.

Figures 9 and 12 both show that a cone shell configuration or a hybrid configuration with a thicker ring performs slightly better in depth sensitivity regardless of the depth of the focal point. This may be explained as follows. For a small depth such as 0.3 mm, the angle between the light beam and the normal axis would be larger when the ring is thicker. The intersection between the cone shell region and the tumor is thus larger as shown in Fig. 15, so the depth sensitivity for tumor measurement will be better. Similarly, for a large depth of the focus such as 1.0 mm, the intersection between the cone shell region and the tissue model is mainly located within the stroma. A thicker ring would mean more contribution from the stroma. It should be pointed out that the interpretation by Figs. 14 and 15 relies on the assumption that photons roughly maintain the original direction before reaching the target region. This is true if the desired depth is comparable to or smaller than the reciprocal of the reduced transport coefficient.

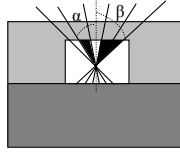


Fig. 15. Intersection of the cone shell region and the tumor when the ring thickness is different. The symbols “ α ” and “ β ” refer to the angles between the light beam and the normal axis for a thin and a thick ring respectively.

Figures 10(a), 11(a) and 13(a) show that a smaller detection fiber performed better for a depth of the focal point at 0.3 mm, which could be explained as follows. The detection fiber can be imaged into the tumor region according to the ray retracing method as shown in Fig. 3. The image of a smaller fiber in the tumor region is more likely to yield photons traveling in the tumor region thus a higher fraction of collisions in the tumor. In contrast, the image of a larger detection fiber is more likely to yield photons traveling in other regions thus a smaller fraction of collisions in the tumor.

Tables 5 and 6 show that the cone shell and hybrid configurations perform better than the cone configuration in terms of sensitivity. For sensitive measurements from tumor, a cone shell configuration and hybrid configuration with a large ring radius yields much better performance than the cone configuration. This could be attributed to the fact that the cone shell configuration and hybrid configuration provides a relatively larger intersection between the cone shell region and the tumor compared to the cone configuration. It should be pointed out that the comparison between the cone shell configuration and the cone configuration is analogous to that between a fiber-optic probe configuration with two obliquely placed fibers and that with two straight fibers [25–27] to certain extent. For sensitive measurements from the stroma, a cone shell configuration or hybrid configuration with a large ring radius yields much better performance than the cone configuration. This is due to the fact that the light beam in the cone shell configuration or hybrid configuration is able to propagate around the finite-width tumor and reach the stroma thus maximizing the contribution of the stroma to measured diffuse reflectance.

Another parameter that may affect simulation results is the emission wavelength. The simulations presented in this report were carried out for a wavelength of 420 nm which is close to the absorption peak of hemoglobin. The scattering coefficient of the tumor and the absorption coefficient of the stroma at 420 nm are particularly high [28, 29], thus an enhanced sensitivity to the embedded tumor and the stroma can be achieved if the optimal configuration was used. At longer wavelengths, the scattering coefficient of the tumor and the absorption coefficient of the stroma would decrease [28, 29]. It is quite likely that it will be more challenging to achieve the enhanced sensitivity to the tumor or the stroma. In that case, a new series of simulations may be needed to find the exact sensitivities.

Although the tumor size was fixed at a small value to represent an early tumor in this study, the rules of thumb for achieving enhanced sensitivity to different regions (but not necessarily every figure) should remain unchanged even if the tumor size changes because they agree with the analysis of illumination and detection geometry based on light propagation as shown in Figs. 14 and 15. They are supported by the previous publications [25, 27, 30, 31] in which fiber-optic probes with related geometries were simulated. The exact sensitivity to each region may change with the tumor size, which can only be obtained by a new batch of simulations.

In this study, the central line of the Lens 2 and Lens 3 (Fig. 1) always overlap with the middle line of the tumor. It can be predicted that the sensitivity to the lesion would decrease when the focal point is located on the margin of a lesion. In a real application, the focal point can be scanned across a tumor in the lateral dimension with a small step size. During scanning, some measurements will be taken from the middle of the lesion and others will be taken from the margin of the lesion or outside the lesion. The difference between these measurements as quantified by “Tumor contrast” defined in Eq. (14) could be used to find the

tumor margin. The optimal configuration identified in this study will maximize such a difference to increase the contrast of the tumor region relative to the normal region.

The method for simulating lens based illumination and detection is generally applicable to any similar lens based setups for optical measurements. In addition, the following rules of thumb can be of general interest to any application in which the high sensitivity to a target tissue region is desirable. Based on the results shown in this report, it can be seen that the two parameters, i.e. the depth of focal point in the tissue model and the cone (in the cone configuration) or ring (in the cone shell configuration) radius, are important to the achievement of sensitive measurements from a given region. To achieve enhanced sensitivity to a target region, the focal point needs to be located in the region. Moreover, a large cone or ring radius, which corresponds to a small f-number for a fixed focal length, would help achieve high sensitivity. These rules of thumb are applicable to a layer tissue model with different optical properties if the desired depth is comparable to or smaller than the reciprocal of the reduced transport coefficient. This condition will ensure that photons roughly maintain the original direction before reaching the target region.

6. Conclusion

We have developed a Monte Carlo based method to investigate depth sensitive diffuse reflectance measurements using a non-contact lens based system in an SCC model. Three lens based configurations, i.e. the traditional cone configuration, a novel cone shell configuration and a hybrid configuration involving the cone shell illumination and the cone detection, were studied using the method. It is shown that depth sensitive measurements were achieved by adjusting the following two parameters: (1) the depth of focal point of the imaging lens in the SCC model; and (2) the cone radius in the cone configuration or the ring radius in the cone shell configuration. It was demonstrated that the cone shell and the hybrid configurations in general have better depth sensitivity than the more commonly used cone configuration for diffuse reflectance measurements in the SCC model. The Monte Carlo method and the findings for different configurations can be useful in guiding the development of a non-contact lens based system for the optical diagnosis of early epithelial cancer.

Acknowledgment

The authors would like to acknowledge the financial support from Tier 1 grant and Tier 2 grant funded by the Ministry of Education in Singapore (Grant nos. RG47/09 and MOE 2010-T2-1-049).